Electronic Supplementary Information

Theoretical Design of 2D *Pca*2_1 SiNOX (X=H, F, and Cl) Phases: A New Family of Flexible Wide Bandgap Semiconductors†

Heng Zhang,[a, b, c] Jiahao Yu,[b] Sylvain Pitié,[c] Frédéric Guégan,[c] Junjie Wang,*[b] Gilles Frapper*[c]

[a]Institute of Semiconductors, Henan Academy of Sciences, Zhengzhou, Henan 450000, People's Republic of China, Email: hengzhang@hnas.ac.cn

[b]State Key Laboratory of Solidification Processing, School of Materials Science and Engineering, Northwestern Polytechnical University, Xi'an, Shaanxi 710072, People's Republic of China

[c]Applied Quantum Chemistry group, E4, IC2MP, UMR 7285 Poitiers University-CNRS, 4 rue Michel Brunet TSA 51106 - 86073 Poitiers Cedex 9, France

*Corresponding authors:

Junjie Wang: wang.junjie@nwpu.edu.cn

Gilles Frapper: gilles.frapper@univ-poitiers.fr

CONTENTS

S1 Methodology

S1.1 DFT calculations (VASP)

Structural optimization. First-principles calculations are performed using the projected-augmented-wave (PAW) method as implemented in VASP (version 5.4.4)[1, 2] Exchange-correlation energy is treated using Perdew-Burke-Ernzerhof (PBE) within the generalized gradient approximation (GGA).[3, 4] A kinetic cutoff energy of 600 eV is used for the wavefunction expansion with a Monkhorst-Pack k mesh grid with a spacing of $2\pi\times0.04$ Å^{-1}. This ensure that enthalpy converges to a criterion lower than 1×10^{-5} eV per cell, and forces to 0.01 eV/Å. The valence electron configurations considered in the calculation are H ($1s^1$), Li ($2s^1$), C($2s^22p^2$), N ($2s^22p^3$), O($2s^22p^4$), F ($2s^22p^5$), Si ($3s^23p^2$), P ($3s^23p^3$), S ($3s^23p^6$), Cl ($3s^23p^5$), Ge ($3d^{10}4s^24p^2$), As ($4s^24p^3$), Se ($4s^24p^4$), Sn ($4d^{10}5s^25p^2$), Sb ($5s^25p^3$), Te ($5s^25p^4$), Pb ($5d^{10}6s^26p^2$), and Bi ($5d^{10}6s^26p^3$). DFT-D3 method was used to take into account of the van der Waals interactions in the bulk van der Waals layered SiNOX phases.[5]

Energy band gap. PBE functional has proven to be accurate for the description of structural properties of materials.[6] In contrast, it may underestimate the value of the band gaps.[7] Therefore, we calculated the band gap at the Heyd-Scuseria-Ernzerhof (HSE06)[8] hybrid functional level of theory, using the optimized PBE structure (single-point energy calculation). This level of theory is noted thereafter as HSE06//PBE. During the band gap calculation of 2D SiNOX material in which the 2D framework extends in the *a*-*c* plane in the three-dimensional lattice, twenty k-points were used between two high-symmetric k-points in the reciprocal space (Γ-Y-T-Z-Γ), i.e., Γ (0 0 0), X(0.5 0 0), T (0.5 0 0.5) and Z (0 0 0.5).

Chemical bonding analysis. To study the chemical bonding, electron localization function (ELF),[9] Manz bond orders,[10] density of states (DOS) and partial (band decomposed) charge density from the optimized geometries from the optimized geometries were also analyzed.

Structural parameters analysis and images. Finally, images of the crystalline structures were produced using VESTA software.[11]

S1.2 Phonon dispersion calculations

In this work, first principles phonon calculations with density functional perturbation theory (DFPT) at a quasi-harmonic level were done using the open-source package PHONOPY (https://phonopy.github.io/phonopy/).[12] Supercells of 2D structures with

displacements were created from a unit cell considering all possible crystal symmetry operations. In general, a 3×3 supercell is sufficient, but larger ones can be required to avoid unphysical imaginary frequencies needed.

S1.3 Mechanical properties

Young's moduli and Poisson's ratio A necessary condition for the thermodynamic stability of a crystal lattice is that the crystal should be mechanically stable with respect to arbitrary (small) homogeneous deformations. Elastic stability criteria for bulk cubic crystals and more different crystal classes was well understood in the work of Born and co-authors.[13, 14, 15] In VASP, IBRION=6 and ISIF≥3 tags allow to calculate the elastic constants. The elastic tensor is determined by performing six finite distortions of the lattice and deriving the elastic constants from the strain-stress relationship.[16]

The elastic matrix of 2D materials was decreased into 3×3 and six elastic constants are C_{11}, C_{12}, C_{22}, C_{16}, C_{26} and C_{66} using the standard Voigt notation:*1*-xx, *2*-yy, *6*-xy. The calculated elastic constants C_{11}, C_{12}, C_{22} and C_{66} in the 2D crystals should satisfy necessary mechanical equilibrium conditions for mechanical stability: $C_{11}C_{22}$-$C_{12}C_{21}$>0 and C_{11}, C_{22}, C_{66}>0.[17]

In terms of these elastic constants, the 2D Young's moduli (in-plane stiffness) for the stain in the [10] and [01] direction are,[18]

$Y_{12} = (C_{11}C_{22}\text{-}C_{12}C_{12})/C_{22}$, (eq.1)

$Y_{21} = (C_{11}C_{22}\text{-}C_{12}C_{12})/C_{11}$. (eq.2)

The corresponding Poisson's ratio are,

$v_{12} = C_{12}/C_{22}$, (eq.3)

$v_{21} = C_{12}/C_{11}$. (eq.4)

In the 2D rectangular crystals, the orientation-dependent Poisson's ratio $v(\theta)$ and Young's modulus $Y(\theta)$ are computed based on the basis of elastic constants and the Poisson's ratio $v(\theta)$ and Young's modulus $Y(\theta)$ along the in-plane θ can be expressed as follows, [19]

$$v(\theta) = \frac{C_{12}\sin^4\theta - B\sin^2\theta\cos^2\theta + C_{12}\cos^4\theta}{C_{11}\sin^4\theta + A\sin^2\theta\cos^2\theta + C_{22}\cos^4\theta}, \quad \text{(eq.5)}$$

$$Y(\theta) = \frac{C_{11}C_{22} - C_{12}C_{21}}{C_{11}\sin^4\theta + A\sin^2\theta\cos^2\theta + C_{22}\cos^4\theta}, \quad \text{(eq.6)}$$

in which A=($C_{11}C_{22}$-$C_{12}C_{21}$)/C_{33}-2C_{12} and B=C_{11}+C_{22}-($C_{11}C_{22}$-$C_{12}C_{21}$)/C_{33}.

Ideal tensile strength For the crystal, the ideal tensile strength is a crucial mechanical parameter, which fundamentally characterizes the nature of the chemical bonding and the elastic limit.[20] To estimate the ideal tensile strength, the strain-stress relation is simulated by applying the uniaxial tensile strain up to ~30% at an increment of 2% along the *a* or the *c* direction, starting with the fully relaxed geometry. Then the ideal strength (the highest strength of a crystal at 0 K) and the critical strain (at which the ideal strength is reached) are determined.[21] The tensile strain is defined as $\varepsilon=a-a_0/a_0$, in which *a* and a_0 are strained and equivalent lattices, respectively. With strain applied in one direction, the lattice constants in the transverse directions and the atom positions are fully relaxed through minimization of the total energy to ensure no stress in the transverse direction. Such relaxation scheme is accomplished by slightly modifying the VASP code with specific constraints of strain components.[22]

S1.4 *Ab initio* molecular dynamics simulations

Thermal stability. *Ab initio* molecular dynamics (AIMD) simulations based on DFT PBE calculations were carried out using VASP code to examine the thermal stabilities of 2D $Pca2_1$ SiNOX (X=H, F, and Cl) structures. AIMD calculations with NVT ensemble and Andersen thermostat were performed at 300 K, 600 K, and 900K.[23] The timestep was 1 *fs*, and the total simulation time was as long as 10 *ps*. In such AIMD simulations, 3×3 supercells of 2D $Pca2_1$ SiNOX (36 formula units, 144 atoms) phases were employed. The Brillouin zone integration was restricted to the Γ point of the supercell, due to a high calculation cost.

S1.5 Lattice thermal conductivity calculations

The lattice thermal conductivity κ_L is calculated by[28, 29]

$$\kappa_L = \sum_{qs} C_v(qs) v_g^2(qs) \tau_{qs} \quad \text{(eq.7)}$$

where $C_v(qs)$ is the specific heat capacity, $v_g^2(qs)$ is the group velocity, and τ_{qs} is the phonon relaxation time. For Callaway model, the phonon relaxation time τ_{qs} is represented as[28]

$$\tau_{qs}^{-1} = \frac{\hbar \gamma_{qs}^2}{\underline{M} \Theta v_g^2(qs)} \omega_{qs}^2 T e^{-\frac{\Theta}{3T}} \quad \text{(eq.8)}$$

in which $\underline{M}$ is the average atomic mass of the surface rhombic cell.

The Grüneisen parameter γ and Debye temperature Θ are given by[28]

$$\gamma_{qs} = -\frac{A}{\omega_{qs}} \frac{d\omega_{qs}}{dA} \quad \text{(eq.9)}$$

$$\Theta^2 = \frac{5\hbar^2}{3k_B{}^2}\frac{\int \omega^2 g_s(\omega)d\omega}{\int g_s(\omega)d\omega}, \quad \text{(eq.10)}$$

in which, $g_s(\omega) = \sum_q \delta(\omega - \omega_{qs})$, A is the cell area, ω_{qs} is the frequency, and $g_s(\omega)$ is the vibrational density of states.

The lattice thermal conductivities (and related calculation parameters) of the 2D materials are related to the effective van der Waals thickness d_v along the vaccum direction, which are given by

$$d_v = d_1 + (d_2 + d_3) \quad \text{(eq.11)}$$

in which, d_1 is the atomic layer thickness and d_2 and d_3 are the *van der Waals* radii of atoms on the upper and lower surfaces of the outmost atomic layers, respectively.[30, 29]

The lattice thermal conductivity κ_L od 2D phases were obtained by solving the Boltzmann transport equation (BTE) in ShengBTE code.[31] The second-order and third-order interatomic force constants (IFCs) are calculated based on the 2×1×2 supercells, and the cutoff radii for the third-order IFCs were set to the range of fourth neighboring atoms. In the current work, the cost-effective scalebroad = 0.5 and the denser 13×13×13 Q grid were adopted in this work.

S2. Bonding of bulk LiSiON

Table S1 Bond Distances and Associated Manz Bond Orders of Various Atomic Pairs in α-LiSiON Phase

Bond type	Bond distance (Å)	Manz bond order
Li-O	1.97 Å	0.12
	1.98 Å	0.11
	1.92 Å	0.13
Li-N	2.35 Å	0.05
Si-N	1.76 Å	0.86
	1.77 Å	0.83
	1.76 Å	0.86
Si-O	1.62 Å	1.16

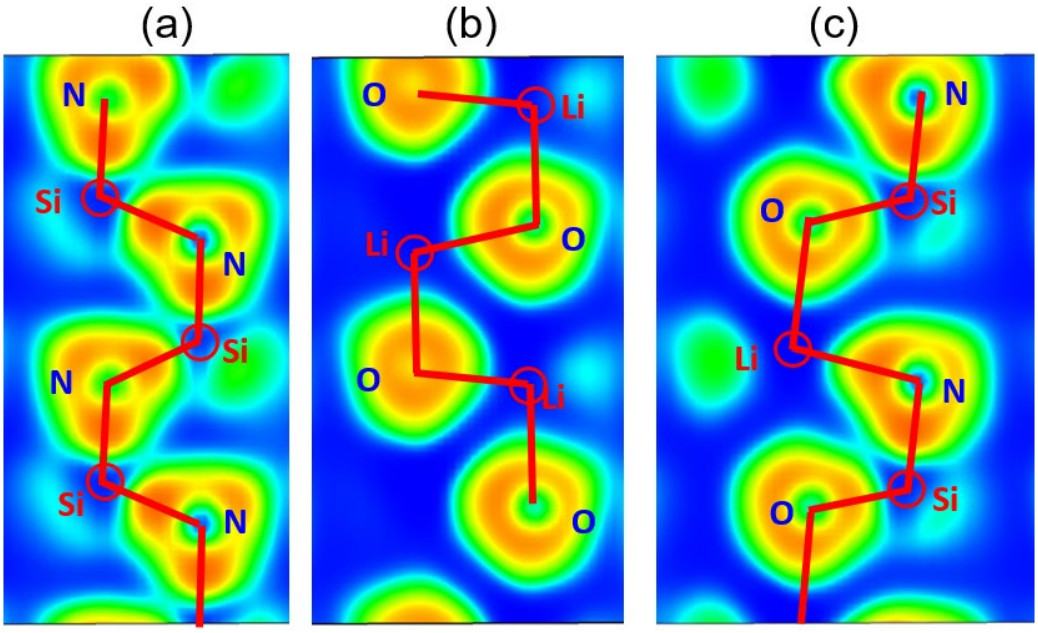

Figure S1 2D ELF contours of bulk α-LiSiON phase with an isovalue of 0.75: (a) (1.1 1 0) plane, (b) (-1.9 1 0) plane, (c) (-1.9 -1 0) plane

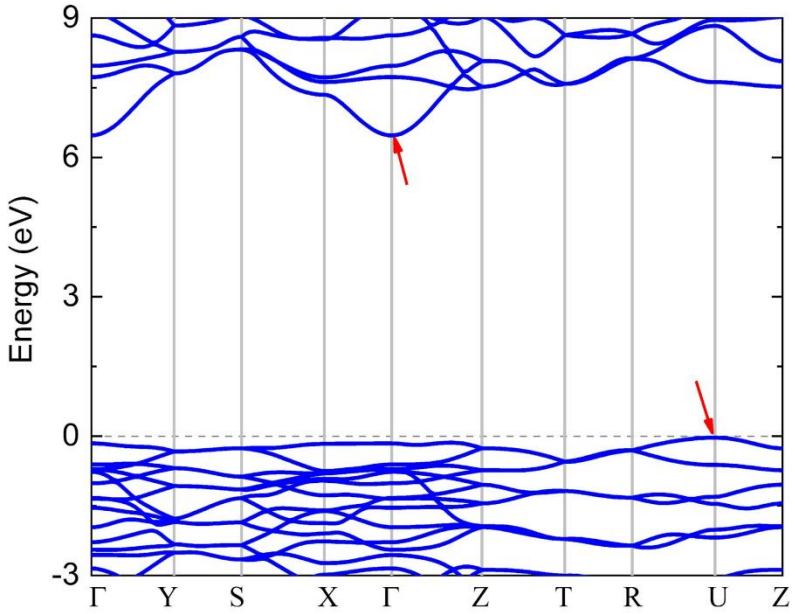

Figure S2 Calculated electronic band structure of bulk α-LiSiON phase by the HSE06//PBE functional.

In Figure S2, the valence band maximum and conduction band minimum are located at U and Γ points, respectively, leading to an indirect band gap of 6.51 eV.

S3. Crystallographic parameters of 2D *Pca*2$_1$ SiNOX

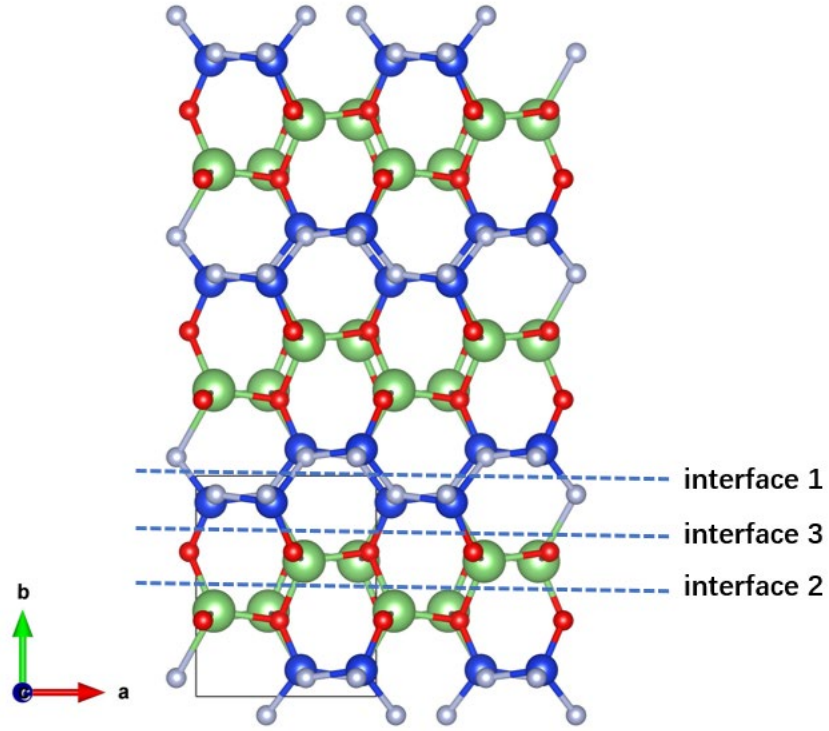

Figure S3 Structure diagram of the interfaces **1**, **2**, and **3** of bulk α-LiSiON. The interface **1** contains only Si-N bonds. The interface **2** contains only Li-O bonds. The interface **3** contains Si-O and Li-N bonds.

Table S2 Crystallographic Parameters of 2D *Pca*2$_1$ SiNOX (X=H, F, and Cl) at the PBE Level of Theory. The corresponding VASP POSCAR formats were provided the last of the ESI.

Phase	Z	Space Group	Lattice parameters (Å,°)	Atomic coordinates (fractional)
SiNOH	4	*Pca*2$_1$ SG 29	*a*=6.62, *b*=35.42, *c*=4.95, *α*=*β*=*γ*=90.0	Si 4a (0.39 0.02 0.55) N 4a (0.37 0.00 0.21) O 4a (0.91 0.94 0.57) H 4a (0.32 0.08 0.43)
SiNOF	4	*Pmc*2$_1$ SG 26	*a*=5.57, *b*=36.25, *c*=4.94, *α*=*β*=*γ*=90.0	Si 4a (0.40 0.02 0.52) N 4a (0.37 0.01 0.18) O 4a (0.02 0.94 0.60)

				H 4a (0.37 0.09 0.46)
SiNOCl	4	$Pca2_1$ SG 29	a=5.48, b=37.00, c=4.93 $\alpha=\beta=\gamma$=90.0	Si 4a (0.41 0.02 0.54) N 4a (0.37 0.01 0.19) O 4a (0.03 0.94 0.61) Cl 4a (0.45 0.09 0.42)

S4. Stability of 2D *Pca*2$_1$ SiNOX

To ascertain the experiment validation of these four predicted 2D *Pca*2$_1$ SiNOX (X=H, F, and Cl), four criteria were investigated to verify their phase viabilities: thermodynamic, dynamic,[12] mechanical,[32] and thermal stabilities.[33]

First, the cohesive energies of these predicted structures with respect to the isolated atoms, were calculated (T = 0 K) and the associated values are 5.20, 4.51, and 4.52 eV/atom for 2D *Pca*2$_1$ SiNOH, SiNOF, and SiNOCl, respectively, which are comparable with those of typical experimentally synthesized 2D nitrides, e.g., 2D AlN and GaN (4.2~5.2 eV/atom).[34] Besides, the formation energies of these four 2D phases with respect to the bulk elemental materials were computed as -1.48, -1.03, and -0.99 eV/atom for 2D *Pca*2$_1$ SiNOH, SiNOF, and SiNOCl, respectively. These exothermic reactions indicate that these four 2D *Pca*2$_1$ SiNOX phases are energetically favorable for synthesis.

Second, a necessary condition for existence of the materials is that the crystal should be mechanically stable with respect to arbitrary (small) homogeneous deformation.[32] The mechanical stabilities of 2D *Pca*2$_1$ SiNOX phases were determined by computing their elastic constants matrix (C_{ij}) that provide crucial information about the elastic deformation behavior of a crystalline structure. The calculated elastic constants of 2D *Pca*2$_1$ SiNOX in Table S3 all satisfy the Born elastic criteria.[17]

Third, the dynamic stabilities of four 2D *Pca*2$_1$ SiNOX phases were examined by phonon dispersion calculations. It can be found in Figure S3 that no imaginary frequency appears in their phonon dispersion curves, indicating the dynamic stabilities of these four 2D *Pca*2$_1$ SiNOX structures.

Lastly, the *sine qua non* condition of a "viable" compound was also examined by performing AIMD simulations at different temperatures (up to 900 K) to verify that our proposed 2D *Pca*2$_1$ SiNOX structures are kinetically and thermally stable. The energy fluctuations, radial distribution functions (RDF), and final snapshots during the AIMD simulations are presented in Figures S4-S12. One can see that the atoms can only vibrate around their equilibrium positions without breaking Si-N, N-O and O-X bonds at 300 K, 600 K, and 900 K, which indicates that these 2D *Pca*2$_1$ SiNOX crystals will not decompose at these temperatures. Then, it can be concluded that these 2D *Pca*2$_1$ SiNOX structures exhibit robust thermal stabilities.

Therefore, these 2D *Pca*2$_1$ SiNOX (X=H, F, and Cl) phases can experimentally exist as the freestanding sheets, due to the good thermodynamical, mechanical, dynamic, and

thermal stabilities.

Table S3 Calculated Elastic Constants of 2D *Pca*2$_1$ SiNOX (X=H, F, and Cl) Phases by the PBE Functional

Phase	C_{11} (N/m)	C_{12} (N/m)	C_{22} (N/m)	C_{33} (N/m)
SiNOH	102.40	20.89	148.45	49.89
SiNOF	95.39	4.87	133.52	55.57
SiNOCl	119.33	23.58	146.53	57.08

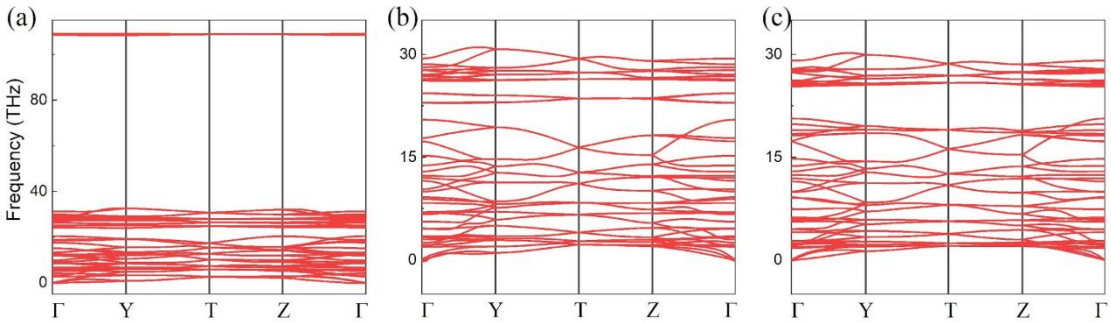

Figure S4 Calculated phonon dispersion curves of 2D *Pca*2$_1$ SiNOX (X=H, F, and Cl) phases by the PBE functional

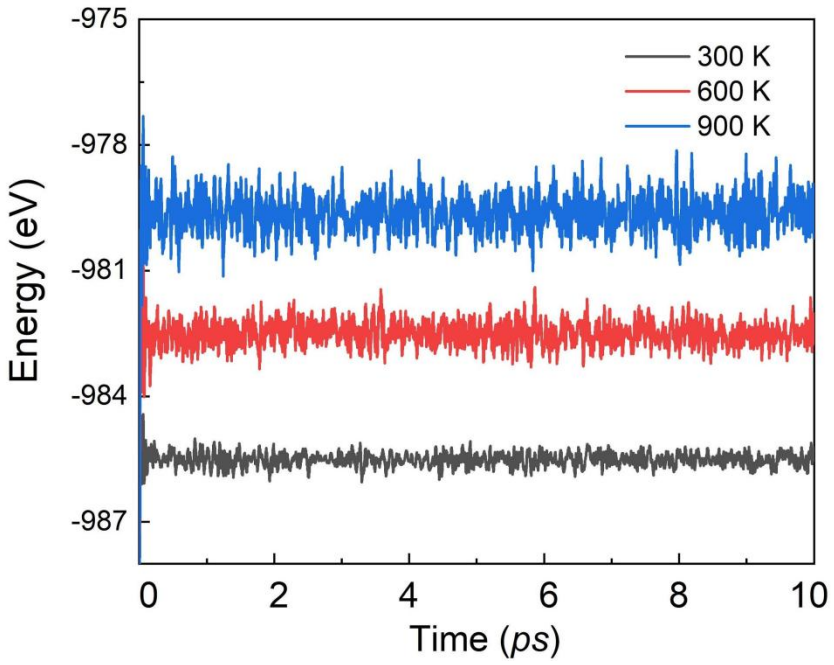

Figure S5 Energy fluctuations of 2D *Pca*2$_1$ SiNOH phases during the AIMD simulations at specific temperatures, T = 300 K, 600 K, and 900 K

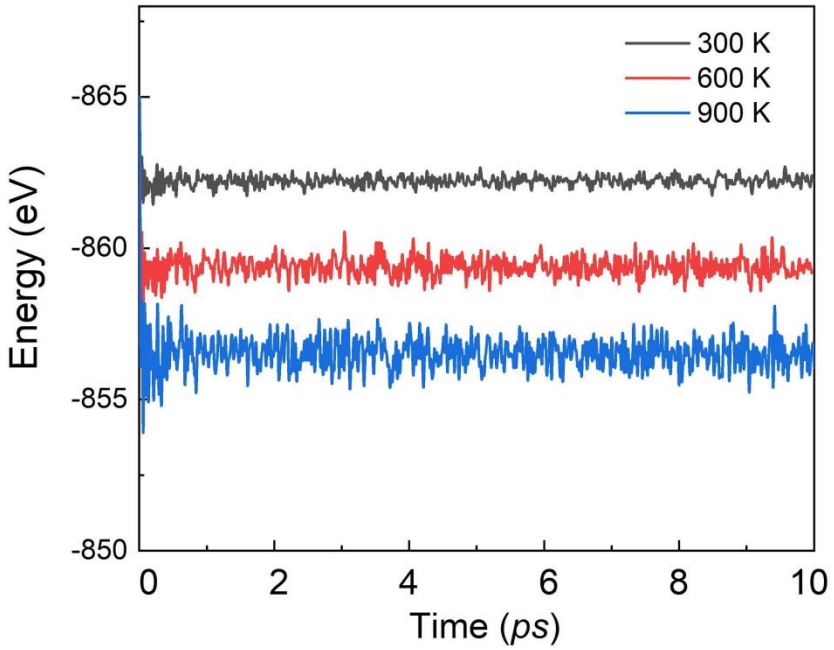

Figure S6 Energy fluctuations of 2D *Pca*2$_1$ SiNOF phases during the AIMD simulations at specific temperatures, T = 300 K, 600 K, and 900 K

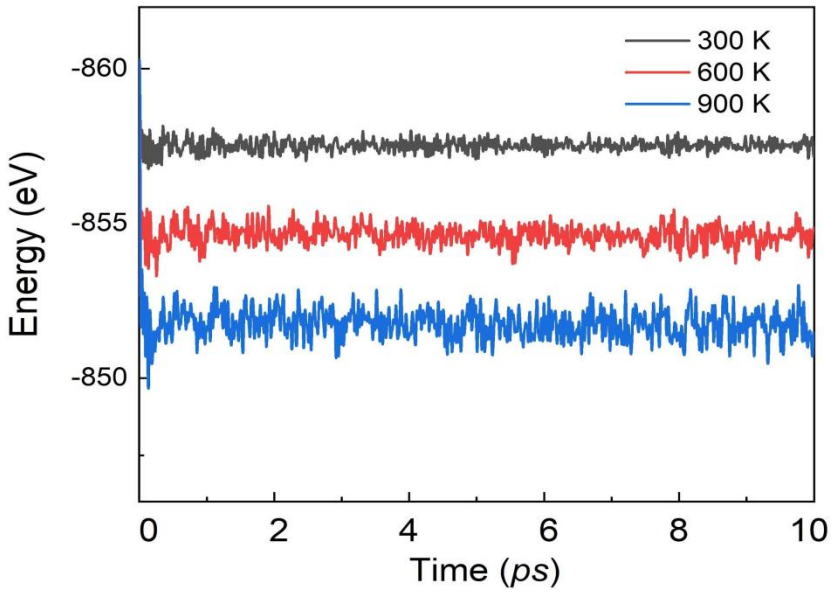

Figure S7 Energy fluctuations of 2D *Pca*2$_1$ SiNOCl phases during the AIMD simulations at specific temperatures, T = 300 K, 600 K, and 900 K

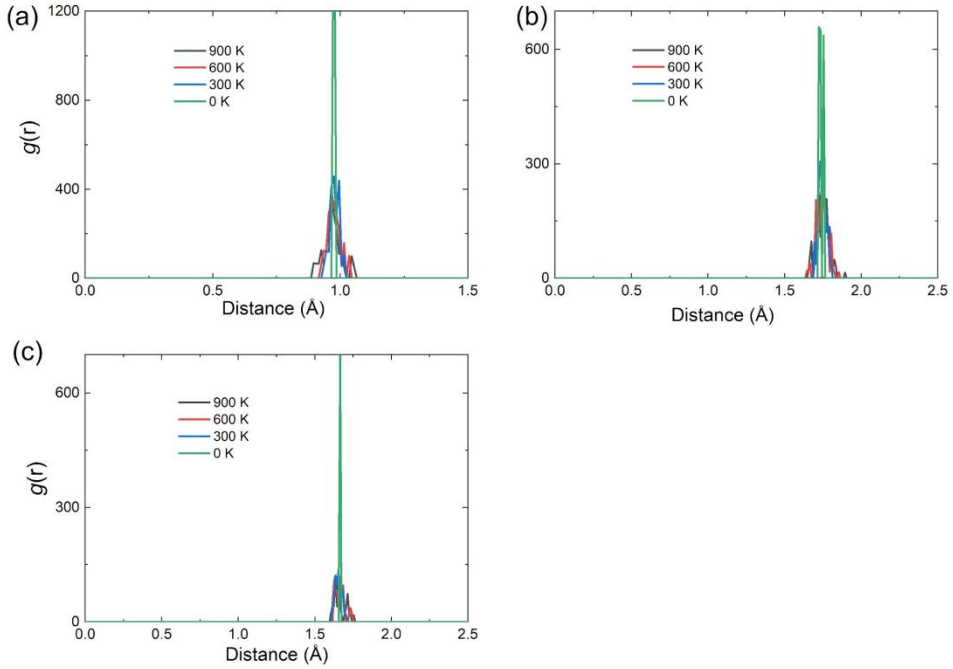

Figure S8 Radial distribution functions $g(r)$ of the O-H (a), Si-O (b) and Si-N (c) separations observed during AIMD simulations at T = 300, 600 and 900 K in the 2D $Pca2_1$ SiNOH

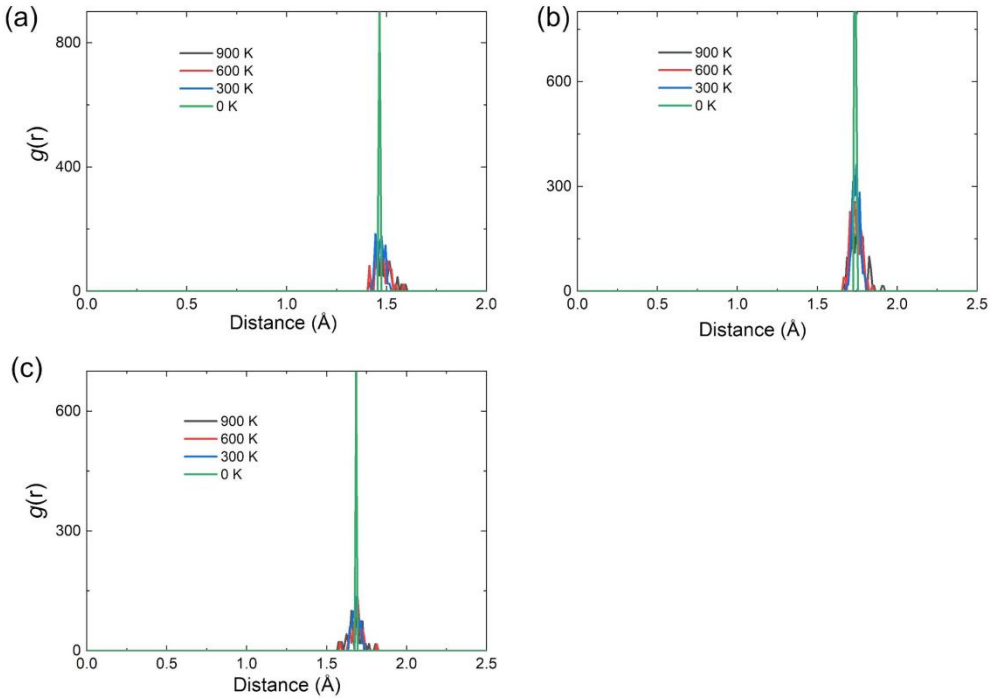

Figure S9 Radial distribution functions $g(r)$ of the O-F (a), Si-O (b) and Si-N (c) separations observed during AIMD simulations at T = 300, 600 and 900 K in the 2D $Pca2_1$ SiNOF

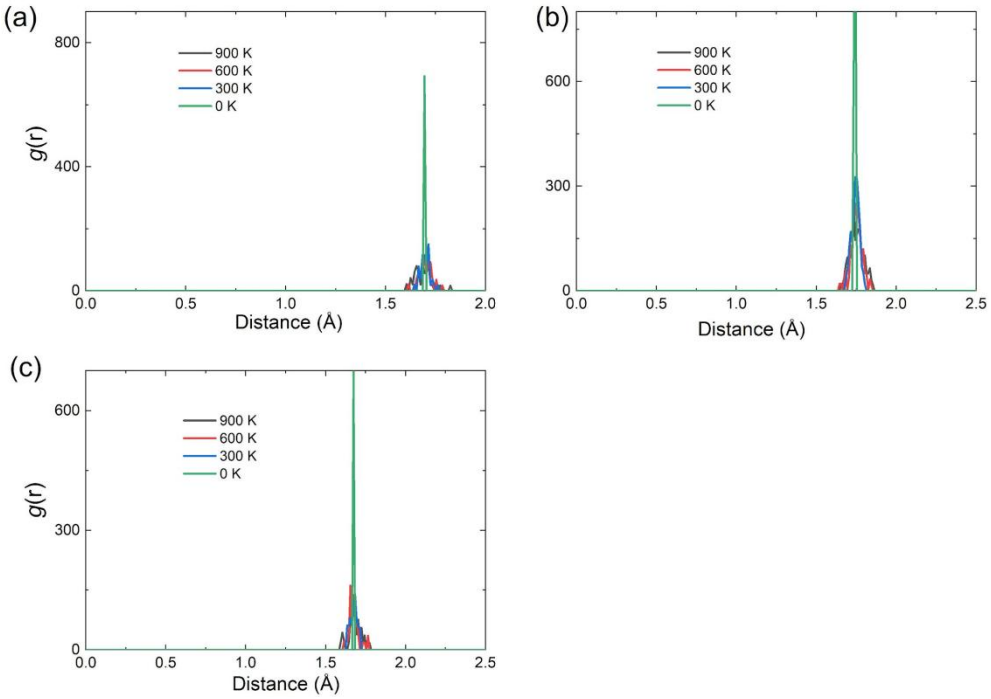

Figure S10 Radial distribution functions $g(r)$ of the O-Cl (a), Si-O (b) and Si-N (c) separations observed during AIMD simulations at T = 300, 600 and 900 K in the 2D $Pca2_1$ SiNOCl

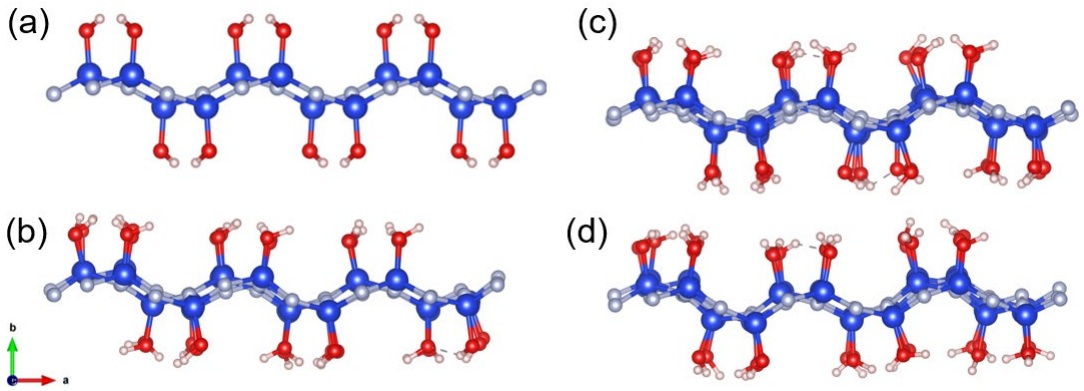

Figure S11 Snapshots of 2D $Pca2_1$ SiNOH supercell (3×3) at ambient pressure at the end of 10 *p*s: (a) 0 K, (b) 300 K, (c) 600 K, and (d) 900K. The silver, blue, red, and pink balls indicate the N, Si, O, and H atoms, respectively.

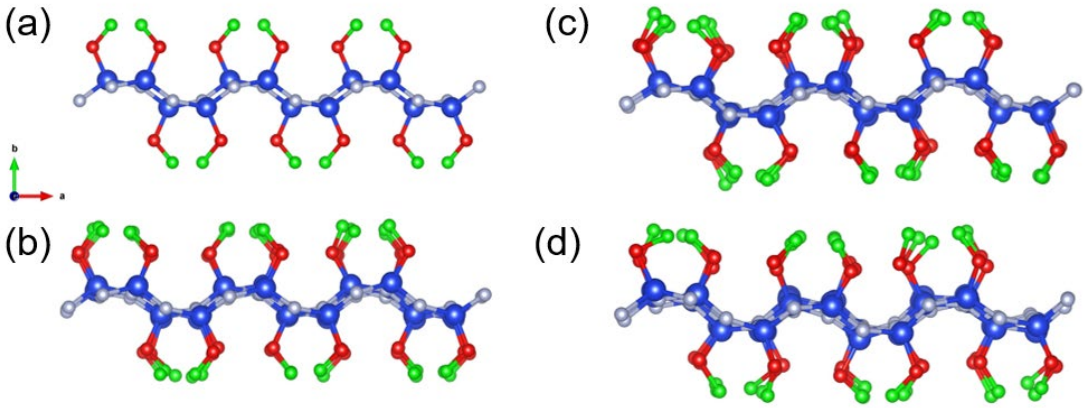

Figure S12 Snapshots of 2D *Pca*2$_1$ SiNOF supercell (3×3) at ambient pressure at the end of 10 *p*s: (a) 0 K, (b) 300 K, (c) 600 K, and (d) 900K. The silver, blue, red, and green balls indicate the N, Si, O, and F atoms, respectively.

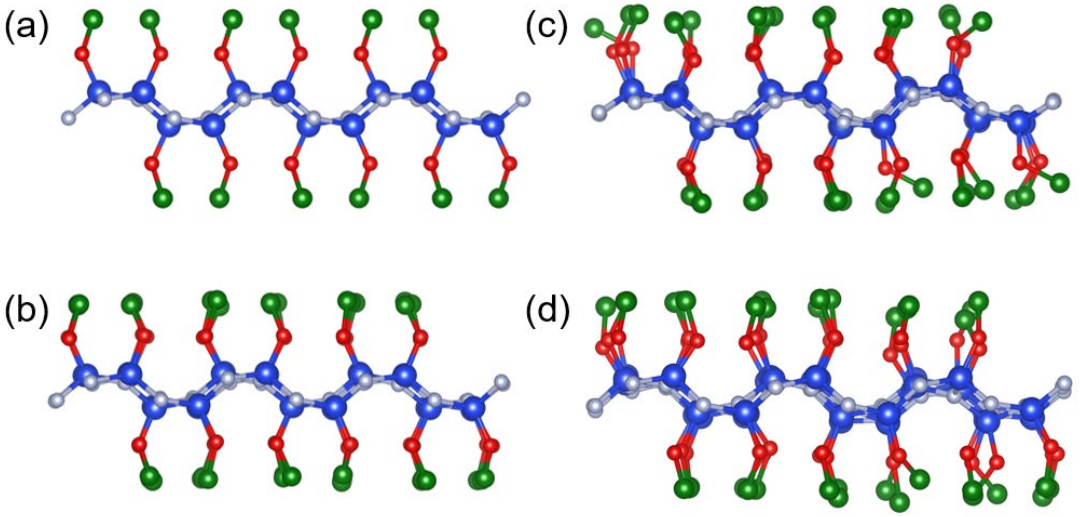

Figure S13 Snapshots of 2D *Pca*2$_1$ SiNOCl supercell (3×3) at ambient pressure at the end of 10 *p*s: (a) 0 K, (b) 300 K, (c) 600 K, and (d) 900K. The silver, blue, red, and dark green balls indicate the N, Si, O, and Cl atoms, respectively.

S5. Dynamical and geometric properties of bulk *Pca*2$_1$ SiNOX

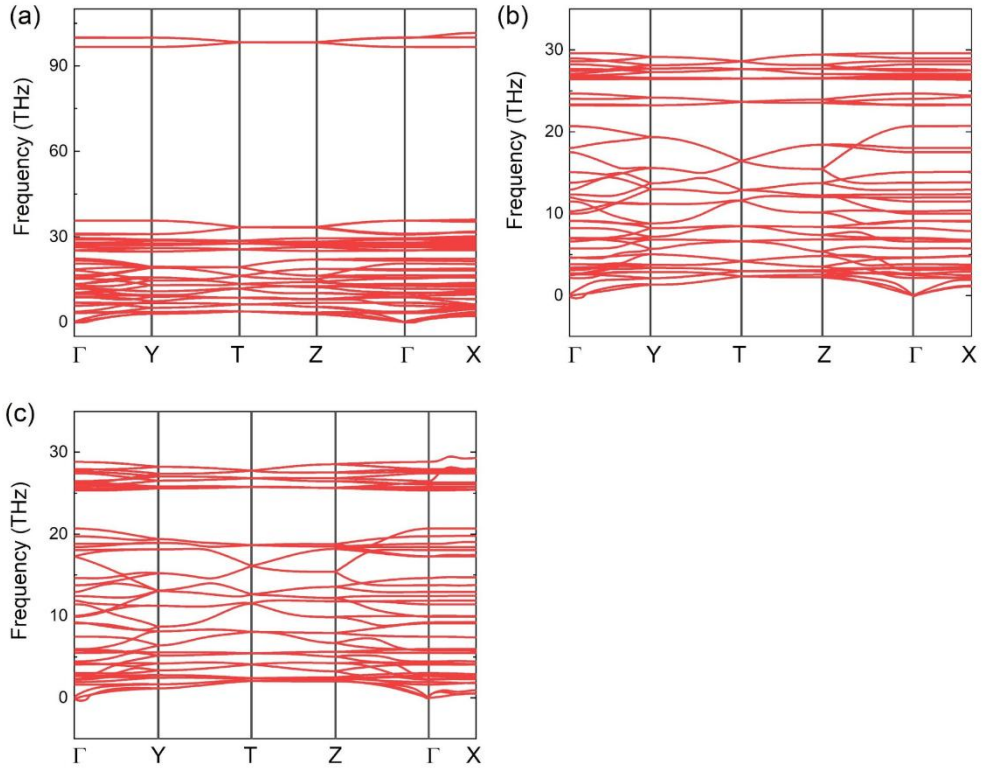

Figure S14 Calculated phonon dispersion curves of bulk *Pca*2$_1$ SiNOH (a), SiNOF (b), and SiNOCl (c) phases by the PBE functional.

In Figure S14, although a slight imaginary phonon mode close to Γ point is found for (b, c), its dynamical stability is still confirmed because it is worth noting that this is a general phenomenon observed in 2D materials, including the well-studied graphene, hexagonal borophene, and CrI_3.[35, 36] The very small region of imaginary frequency (shown as negative) near the Γ point is an artifact from the Fourier interpolation, as discussed in reference 37. Therefore, the bulk *Pca*2$_1$ SiNOH, SiNOF, and SiNOCl are all dynamically stable.

Table S4 Crystallographic Parameters of Bulk $Pca2_1$ SiNOX (X=H, F, and Cl) at the DFT-D3 Level of Theory

Phase	Z	Space Group	Lattice parameters (Å,°)	Atomic coordinates (fractional)
SiNOH	4	$Pca2_1$ SG 29	a=5.47, b=5.92, c=4.81, $\alpha=\beta=\gamma$=90.0	Si 4a (0.41 0.12 0.54) N 4a (0.37 0.05 0.19) O 4a (0.98 0.62 0.59) H 4a (0.48 0.47 0.43)
SiNOF	4	$Pmc2_1$ SG 26	a=5.51, b=7.62, c=4.90, $\alpha=\beta=\gamma$=90.0	Si 4a (0.40 0.08 0.52) N 4a (0.37 0.04 0.17) O 4a (0.02 0.72 0.59) H 4a (0.37 0.40 0.46)
SiNOCl	4	$Pca2_1$ SG 29	a=5.40, b=9.35, c=4.84 $\alpha=\beta=\gamma$=90.0	Si 4a (0.41 0.07 0.53) N 4a (0.37 0.04 0.18) O 4a (0.04 0.77 0.61) Cl 4a (0.47 0.37 0.42)

S6. Geometrical and electronic properties of 2D and bulk *Pca*2$_1$ SiNOX

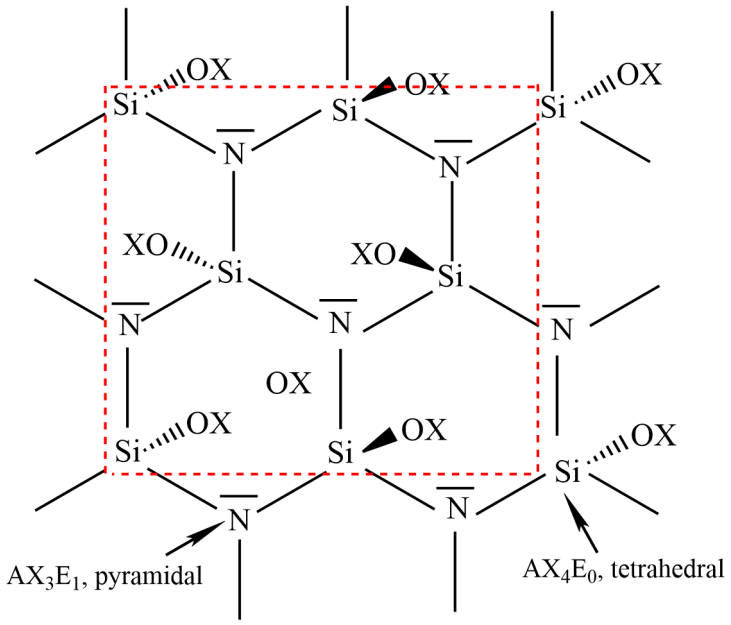

Figure S15 Resonant Lewis structure for repeated unit in 2D *Pca*2$_1$ SiNOX, containing Si: AX_4E_0 and N: AX_3E_1 centers. The unitcell is indicated in the red rectangle.

Table S5 The Summary of Geometrical Parameters Such as Si-N, Si-O, and O-X Bond Distance (Å) and Nitrogen Pyramidalization Angle t_N (°) of Bulk α-LiSiON and 2D *Pca*2$_1$ SiNOX (X=H, F, and Cl)

	bulk LiSiON	2D SiNOH	2D SiNOF	2D SiNOCl
X	Li	H	F	Cl
Si-N (Å)	1.76, 1.76, 1.77	1.73, 1.74, 1.75	1.74, 1.74, 1.74	1.74, 1.75, 1.75
Si-O (Å)	1.62	1.66	1.68	1.67
O-X (Å)	1.92, 1.97, 1.98	0.98	1.47	1.70
t_N (°)	101.6	92.3	94.0	95.4

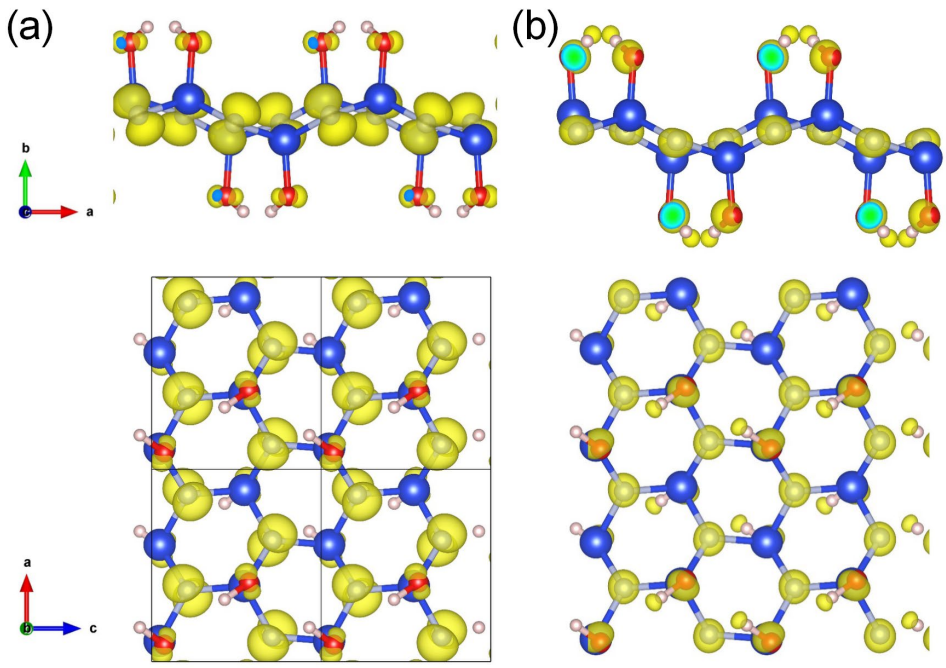

Figure S16 Partial (band decomposed) charge density at VBM (a) and CBM (b) in 2D *Pca*2$_1$ SiNOH. The blue, silver, red and pink balls are Si, N, O and H atoms, respectively.

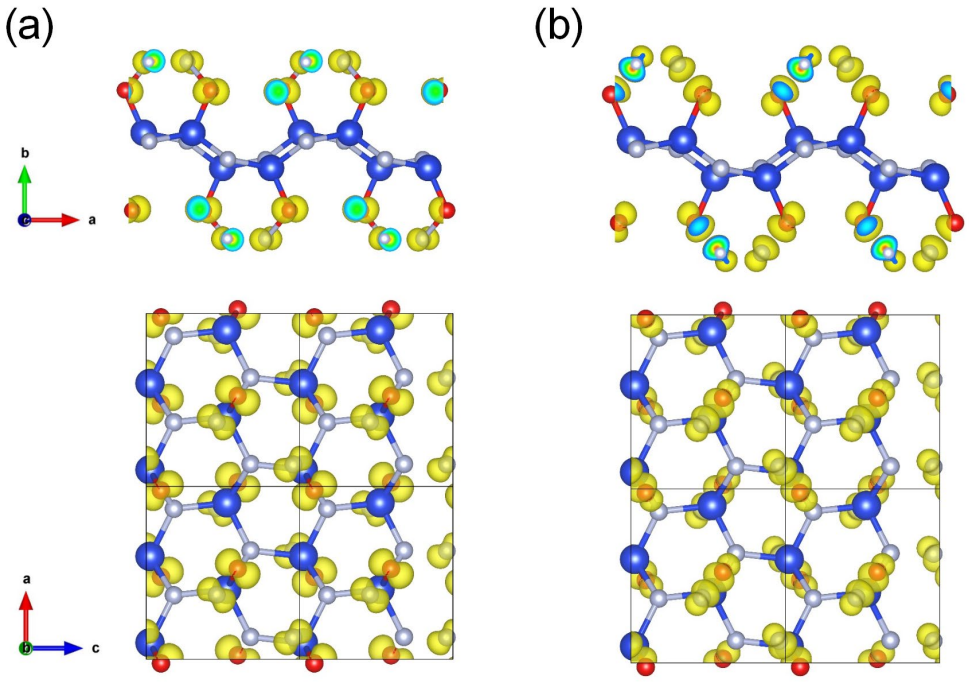

Figure S17 Partial (band decomposed) charge density at VBM (left) and CBM (right) in 2D *Pca*2$_1$ SiNOF. The blue, silver, red and yellow balls are Si, N, O and F atoms, respectively.

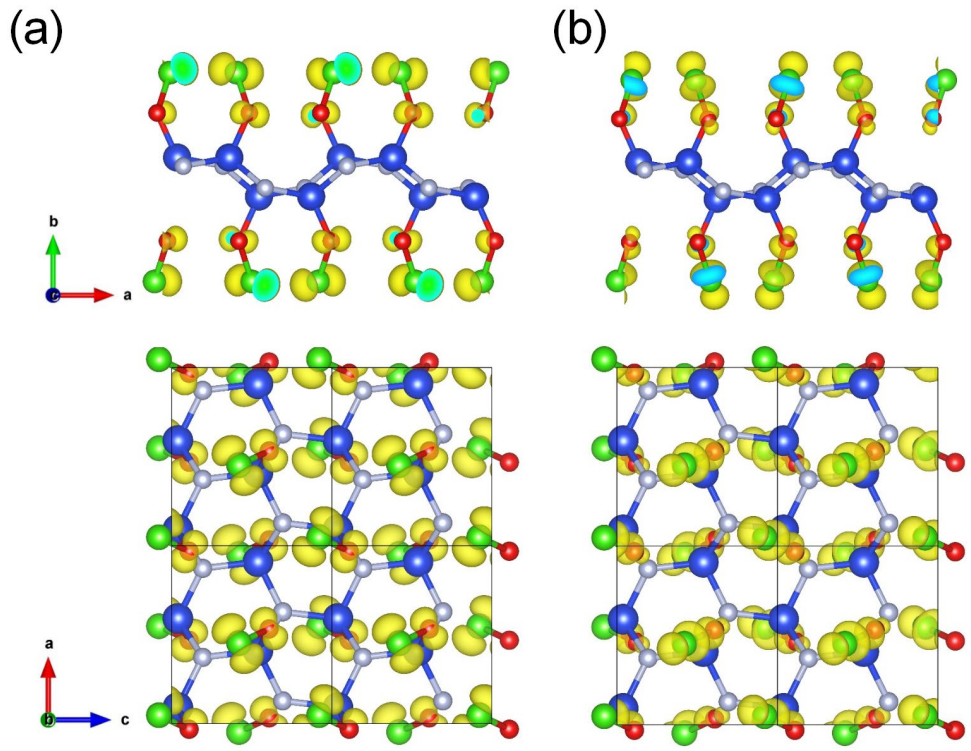

Figure S18 Partial (band decomposed) charge density at VBM (left) and CBM (right) in 2D *Pca*2$_1$ SiNOCl. The blue, silver, red and green balls are Si, N, O and Cl atoms, respectively.

Table S6 Manz Bond Orders of Various Atomic Pairs in 2D *Pca*2$_1$ SiNOX (X=H, F, and Cl). The Bond Distances were Indicated in the Bracket.

	Manz bond order		
	Si-N	Si-O	O-X
SiNOH	0.93 (1.73 Å) 0.91 (1.74 Å) 0.87 (1.75 Å)	0.94 (1.66 Å)	0.79 (0.98 Å)
SiNOF	0.88 (1.74 Å) 0.91 (1.74 Å) 0.90 (1.74 Å)	0.88 (1.69 Å)	0.90 (1.47 Å)
SiNOCl	0.87 (1.75 Å) 0.91 (1.74 Å)	0.87 (1.67 Å)	1.16 (1.70 Å)

	0.89 (1.75 Å)		

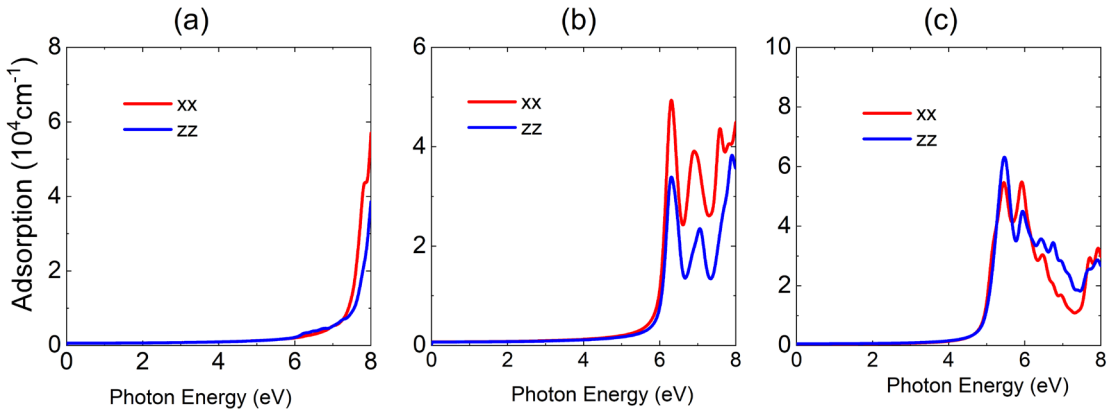

Figure S19 The calculated optical absorptions of 2D (a)*Pca*2$_1$ SiNOH, (b) *Pca*2$_1$ SiNOF, and (c) *Pca*2$_1$ SiNOCl along in-plane spatial directions

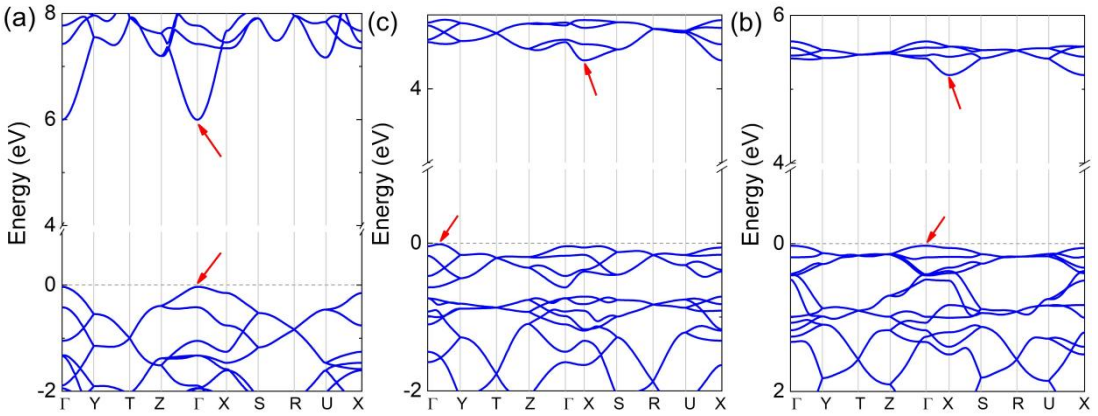

Figure S20 Band structures of bulk *Pca*2$_1$ SiNOX phases within the HSE06//PBE level of theory: (a) SiNOH, (b) SiNOF, and (c) SiNOCl. The valence band maximum and conduction band minimum of bulk *Pca*2$_1$ SiNOX phases are indicated by the red arrows.

In the Figure S20, the band gaps of bulk *Pca*2$_1$ SiNOH, SiNOF, and SiNOCl are 6.03 (direct), 5.22 (indirect), and 4.40 (indirect) eV, respectively.

S7. Mechanical and piezoelectric properties of 2D *Pca*2$_1$ SiNOX

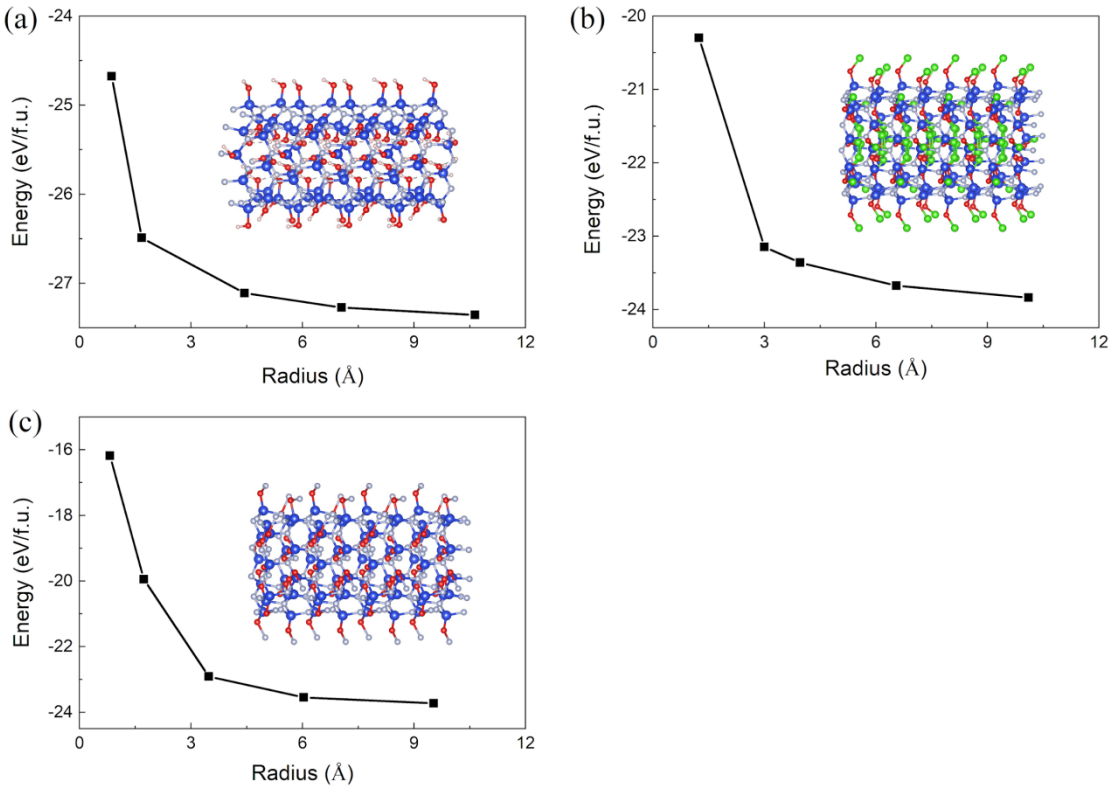

Figure S21 Energy per formula unit of (a) SiNOH, (b) SiNOF, and (c) SiNOCl, nanotubes as a function of the radius. In each panel, the side view of an example of related nanotube was shown.

S8. Lattice thermal conductivity of 2D *Pca*2$_1$ SiNOX

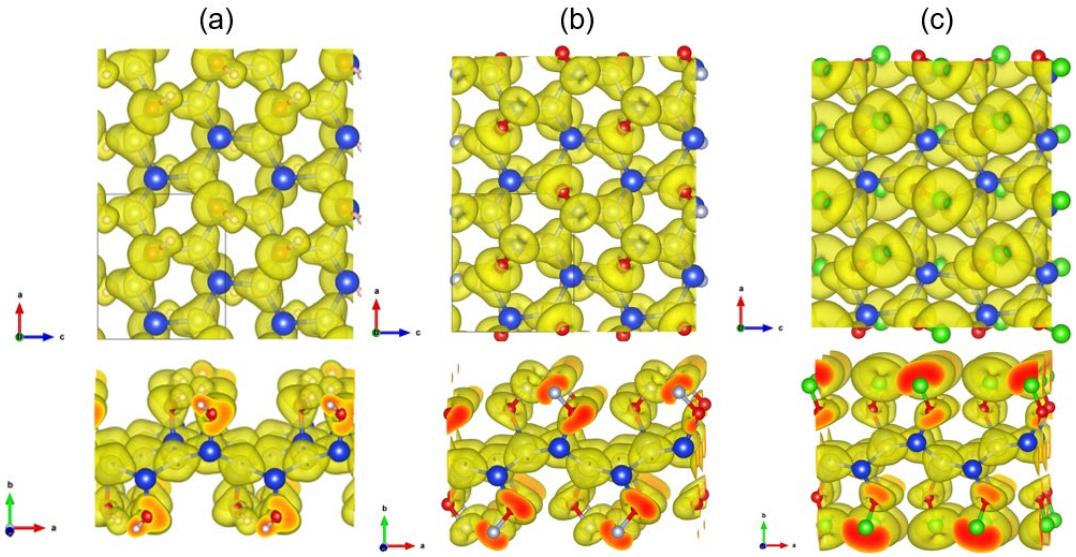

Figure S22 ELF contours of 2D *Pca*2$_1$ SiNOX (X=H, F, and Cl) phases with an isovalue of 0.75: (a) SiNOH, (b) SiNOF, and (c) SiNOCl

Here we chose 2D *Pca*2$_1$ SiNOH as an example for the convergence of the scalebroad value and Q-grid density and the results were depicted in Figure S23. First, the third-order interatomic force constant (IFCs) of 2D *Pca*2$_1$ SiNOH was calculated with a cutoff radius of 0.5 nm. Figure S23(a) shows the results of the convergence test for the lattice thermal conductivity (κ_L) of 2D *Pca*2$_1$ SiNOH with respect to the scalebroad parameter. The results indicate that this parameter exhibits a low deviation of less than 1.06% when scalebroad > 0.5. Second, the convergence test for the Q-grid was presented in Figure S23(b), where the maximum deviation is less than 0.05% when the Q-grid density exceeds 21 × 21 × 1. After conducting a series of test calculations, we selected a scalebroad value of 0.5 and a Q-grid density of 21 × 21 × 1 points for all subsequent work.

As a final verification, we calculated the lattice thermal conductivity (κ_L) of 2D *Pca*2$_1$ SiNOH at 300 K, yielding a value of 0.472 W/mK (0.486 W/mK) for *a*-axis (*c*-axis), which is very close to 0.480 W/mK (0.498 W/mK) and 0.468 W/mK (0.479 W/mK) at the cutoff radius of 0.4 nm and 0.6 nm, respectively, indicating that the cutoff radius of 0.5 nm is sufficient. Therefore, it can be concluded that our method for

calculating thermal transport properties is effective.

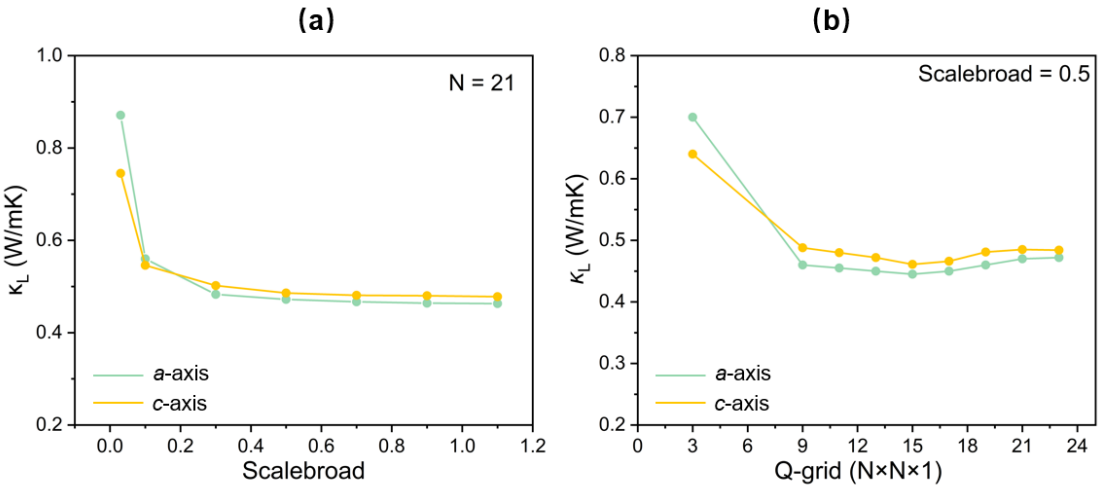

Figure S23 Convergence test results of the lattice thermal conductivity of 2D *Pca*2$_1$ SiNOH with regard to the (a) scalebroad parameter, and (b) Q-grid density

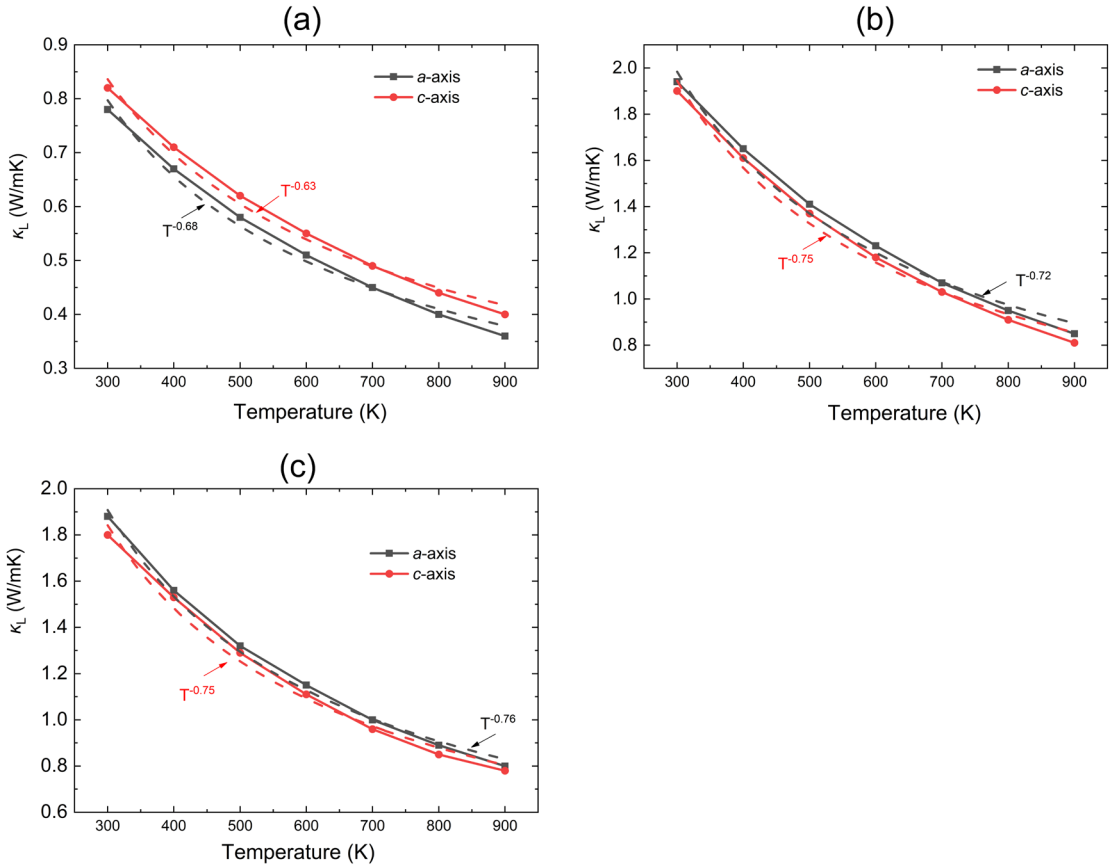

Figure S24 Temperature dependence of the lattice thermal conductivity of 2D *Pca*2$_1$ SiNOX (X=H, F, and Cl) phases: (a) SiNOH, (b) SiNOF, and (c) SiNOCl. The fitting

curves are plotted in dashed lines.

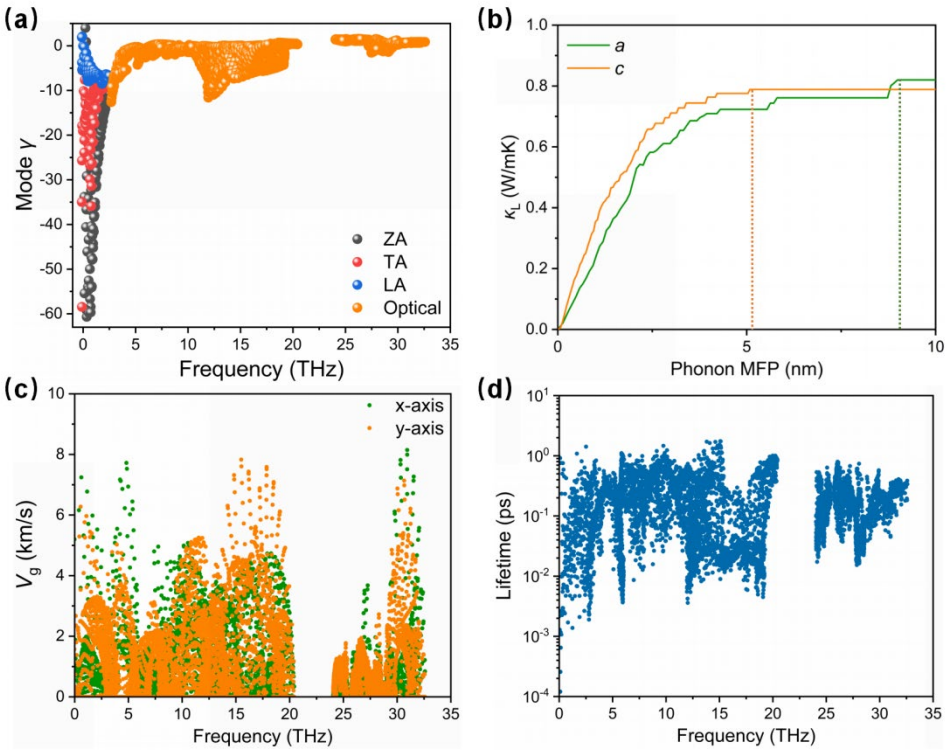

Figure S25 Lattice thermal conductivity of 2D *Pca*2_1 SiNOH: (a) Mode Grüneisen parameter γ as a function of frequency; (b) Normalized integration of the lattice thermal conductivity with respect to the phonon mean free path MFP at 300 K; (c) Group velocities V*g* of the phonons as a function of frequency; (d) Phonon relaxation time as a function of frequency.

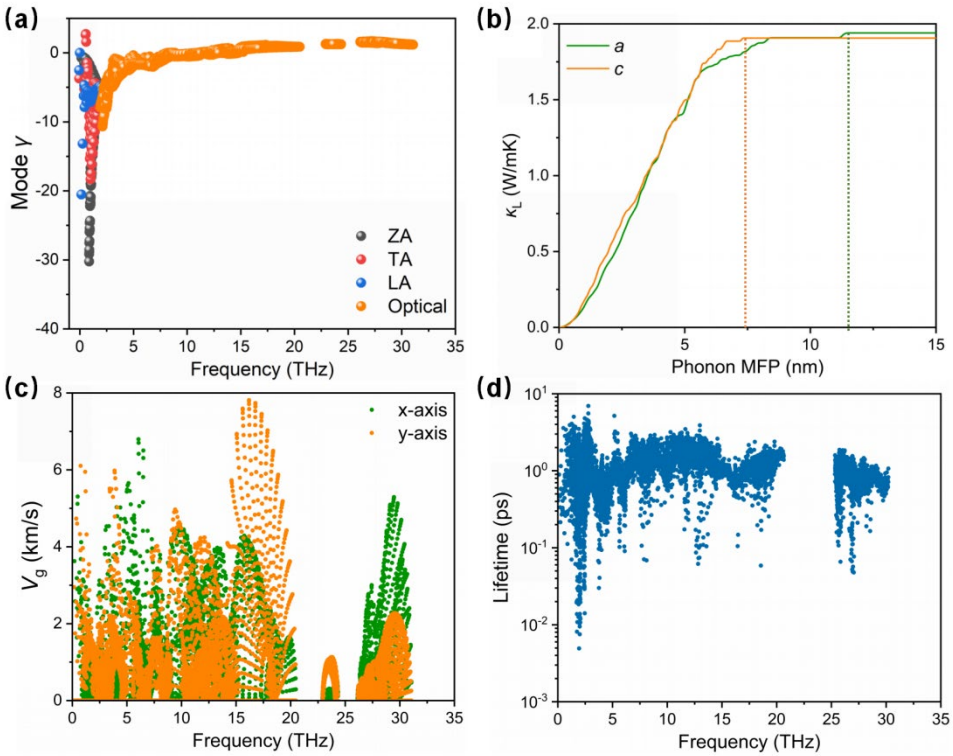

Figure S26 Lattice thermal conductivity of 2D *Pca*2$_1$ SiNOF: (a) Mode Grüneisen parameter γ as a function of frequency; (b) Normalized integration of the lattice thermal conductivity with respect to the phonon mean free path MFP at 300 K; (c) Group velocities V*g* of the phonons as a function of frequency; (d) Phonon relaxation time as a function of frequency.

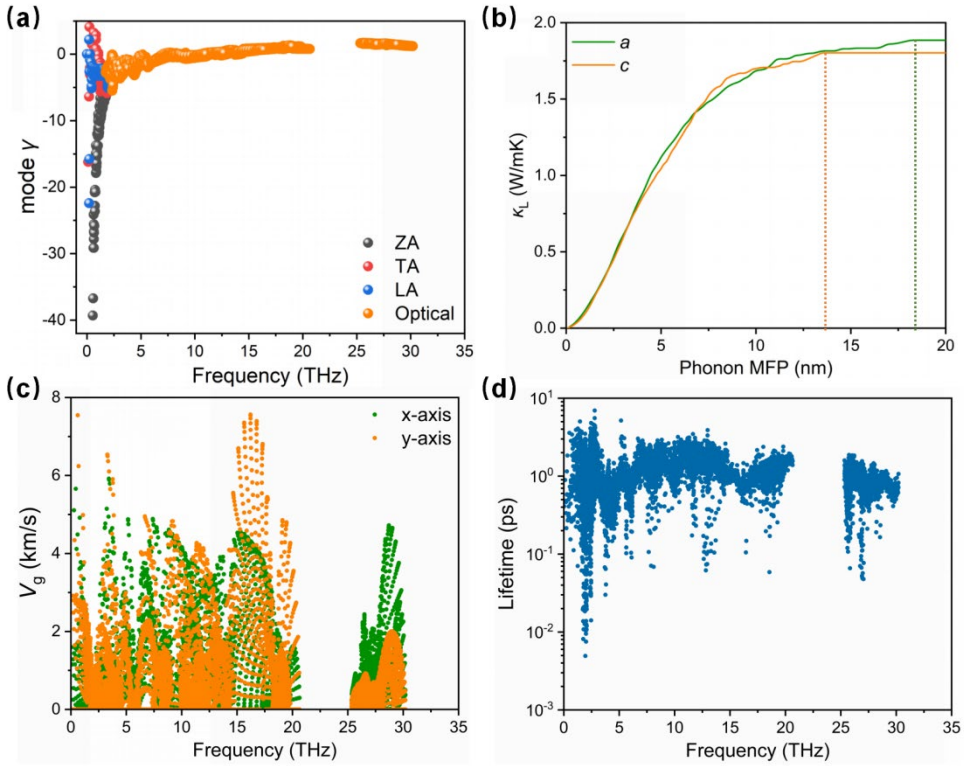

Figure S27 Lattice thermal conductivity of 2D *Pca*2$_1$ SiNOCl: (a) Mode Grüneisen parameter γ as a function of frequency; (b) Normalized integration of the lattice thermal conductivity with respect to the phonon mean free path MFP at 300 K; (c) Group velocities V*g* of the phonons as a function of frequency; (d) Phonon relaxation time as a function of frequency.

S9. Isovalent compounds of 2D *Pca*2$_1$ SiNOX

It's noted that after structure relaxation, the isovalent compounds of 2D PbNOH, SiSbOF, SiBiOF, and SiBiOCl cannot maintain the structure prototype of 2D *Pca*2$_1$ SiNOF and then the phonon curves of 2D PbNOH, SiSbOF, SiBiOF, and SiBiOCl are not presented here.

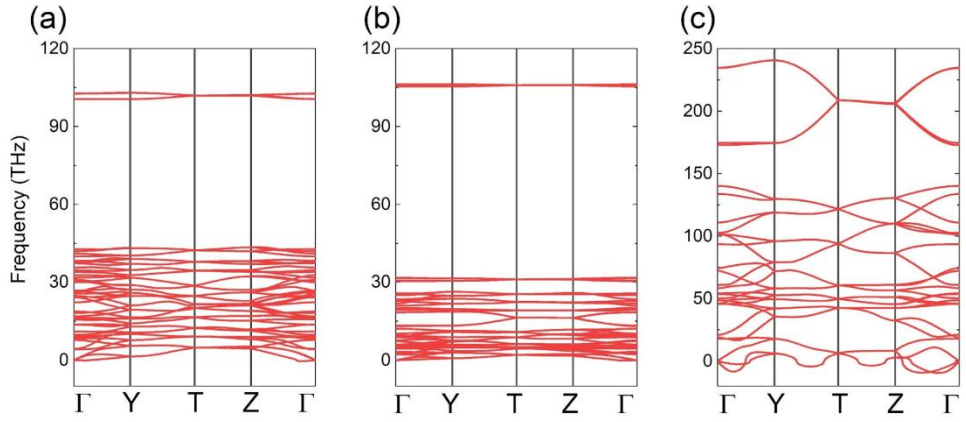

Figure S28 Calculated phonon dispersion curves of 2D *Pca*2$_1$ CNOH (a), GeNOH (b), and SnNOH (c) by the PBE functional

In the Figure S28, the imaginary modes (>1THz) in (c) indicate the dynamic instabilities of 2D *Pca*2$_1$ SnNOH.

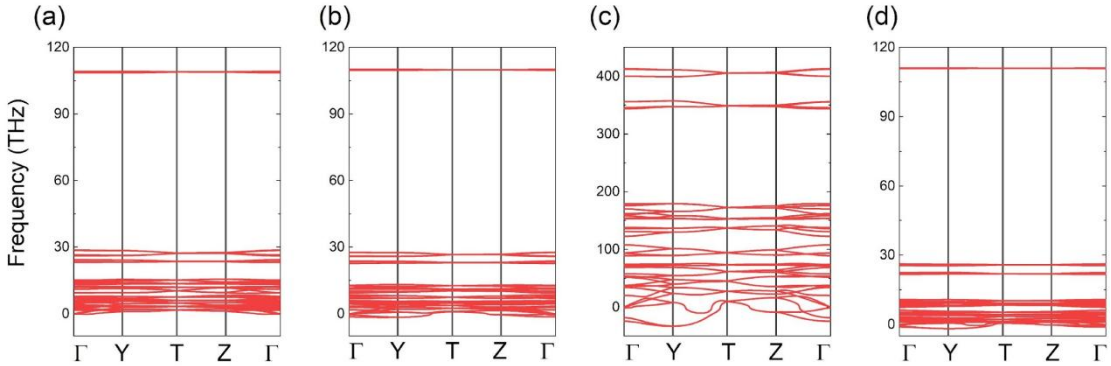

Figure S29 Calculated phonon dispersion curves of 2D *Pca*2$_1$ SiPOH (a), SiAsOH (b), SiSbOH (c), and SiBiOH (d) by the PBE functional

In the Figure S29, the imaginary modes (>1THz) in (b, c and d) indicate the dynamic instabilities of 2D *Pca*2$_1$ SiAsOH, SiSbOH and SiBiOH.

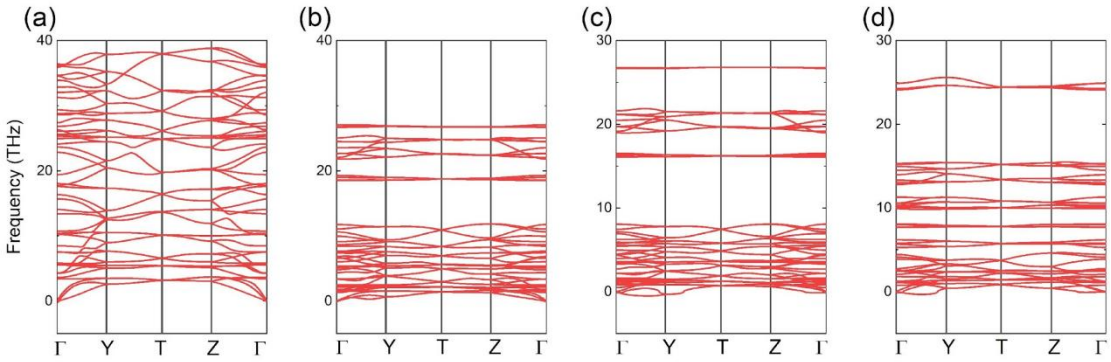

Figure S30 Calculated phonon dispersion curves of 2D *Pca*2$_1$ CNOF (a), GeNOF (b), SnNOF (c), and SiPOF (d) by the PBE functional

In the Figure S30, although a slight imaginary phonon mode close to Γ point is found for (c, d), their dynamical stabilities are still confirmed because it is worth noting that this is a general phenomenon observed in 2D materials, including the well-studied graphene, hexagonal borophene, and CrI_3.[35, 36] The very small region of imaginary frequency (shown as negative) near the Γ point is an artifact from the Fourier interpolation, as discussed in reference 37.[37]

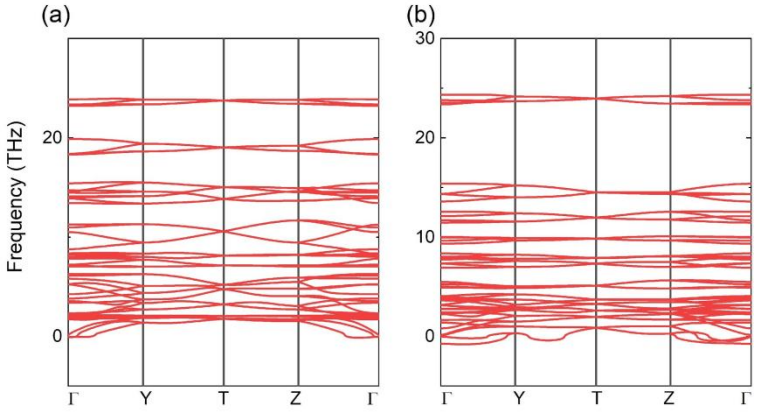

Figure S31 Calculated phonon dispersion curves of 2D *Pca*2$_1$ SiPOF (a) and SiAsOF (b) by the PBE functional

The large imaginary modes in the Figure S31(b) indicate the dynamic instability of 2D *Pca*2$_1$ SiAsOF.

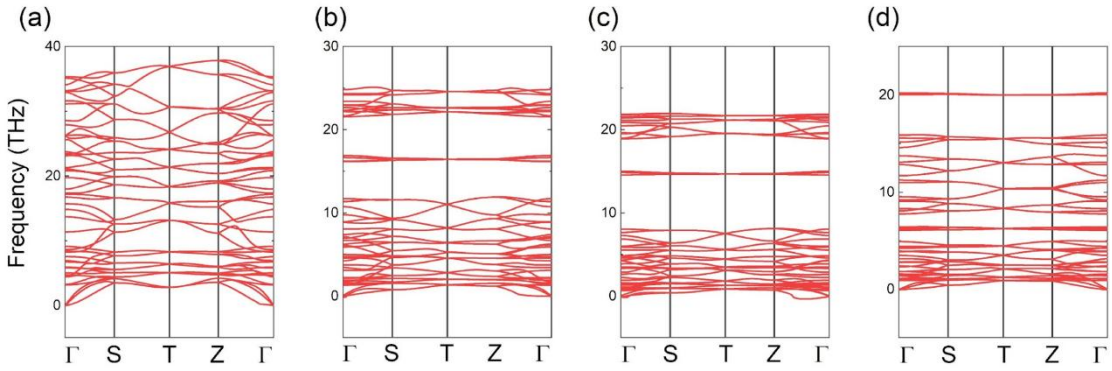

Figure S32 Calculated phonon dispersion curves of 2D *Pca*2$_1$ CNOCl (a), GeNOCl (b), SnNOCl (c), and PbNCl (d) by the PBE functional

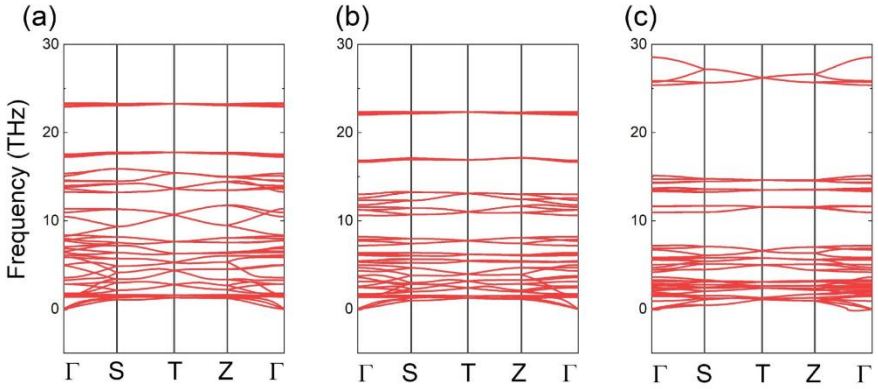

Figure S33 Calculated phonon dispersion curves of 2D *Pca*2$_1$ SiPOCl (a), SiAsOCl (b), and SiSbOCl (c) by the PBE functional

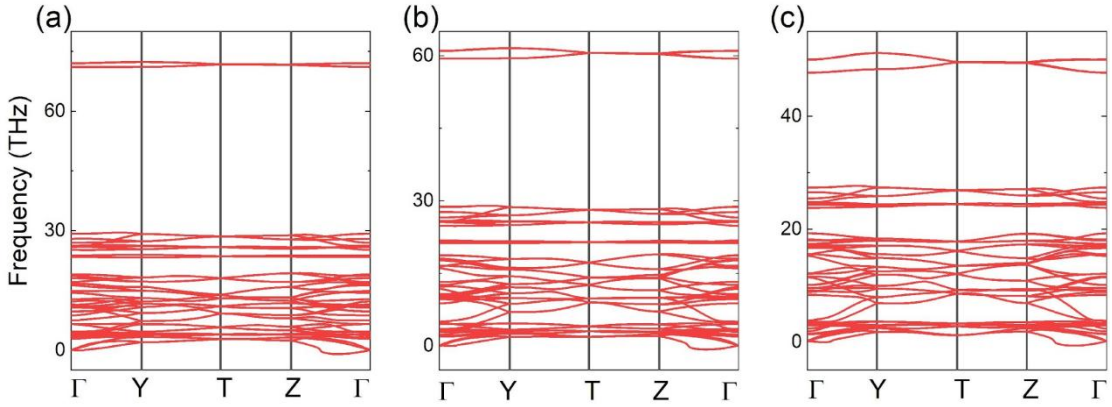

Figure S34 Calculated phonon dispersion curves of 2D *Pca*2$_1$ SiNSH (a), SiNSeH (b), and SiNTeH (c) by the PBE functional

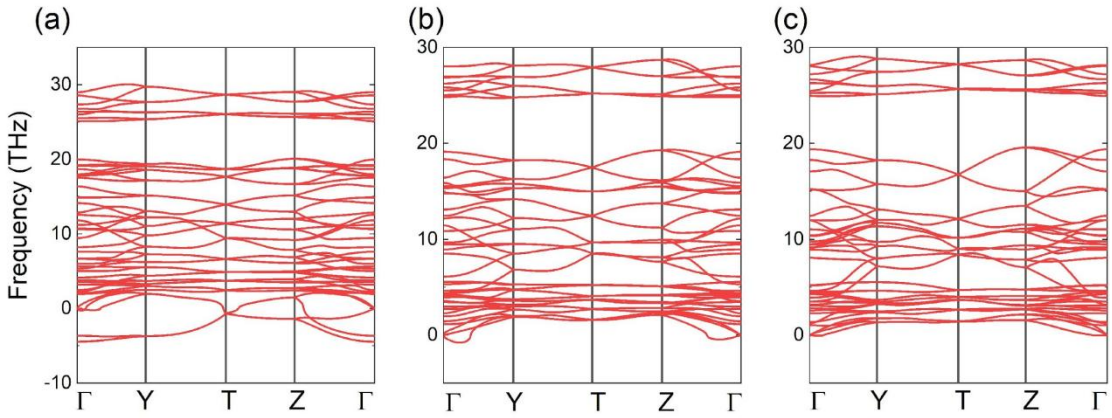

Figure S35 Calculated phonon dispersion curves of 2D *Pca*2$_1$ SiNSF (a), SiNSe (b), and SiNTeF (c) by the PBE functional

In the Figure S35 (a), the large imaginary modes indicate the dynamic instability of 2D *Pca*2$_1$ SiNSF.

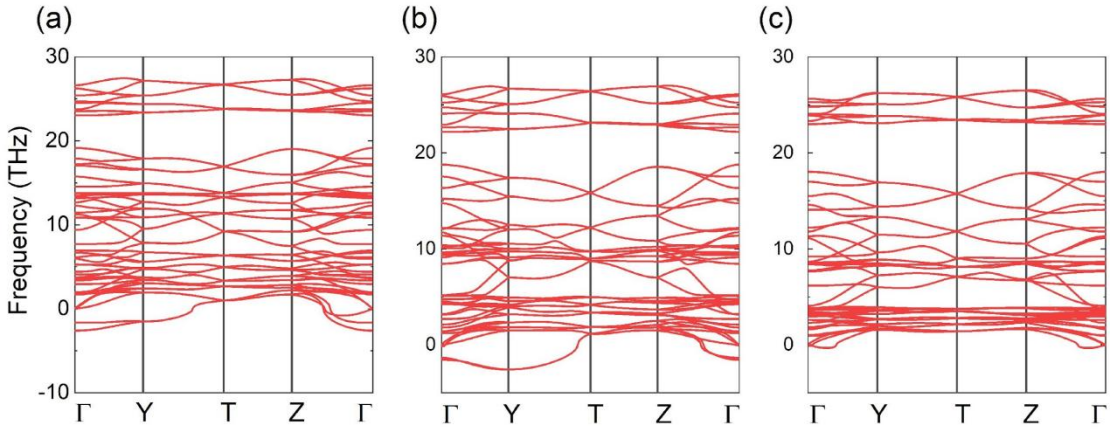

Figure S36 Calculated phonon dispersion curves of 2D *Pca*2$_1$ SiNSCl (a), SiNSeCl (b), and SiNTeCl (c) by the PBE functional

In the Figure S36 (a, b), the large imaginary modes indicate the dynamic instabilities of 2D *Pca*2$_1$ SiNSCl and SiNSeCl.

Table S7 Formation Energies, Bandgaps, and N/P/As/Sb/Bi Pyramidalization Angles t (°) of Isovalent Compounds of 2D $Pca2_1$ SiNOX at the PBE and HSE06//PBE Level of Theory

Phase	Formation Energy (eV/atom)	Bandgap (eV)			t (°)
		PBE	HSE06//PBE		
CNOH	-0.50	5.04	6.64	direct	91.7
SiNOH	-1.48	4.77	6.33	direct	92.3
GeNOH	-0.81	3.07	4.41	direct	96.1
SiPOH	-1.98	2.46	2.80	direct	114.8
CNOF	-0.71	3.74	6.27	direct	97.7
SiNOF	-1.03	3.36	5.88	direct	94.0
GeNOF	-0.39	2.78	4.70	direct	94.5
SnNOF	-0.18	1.19	2.45	direct	93.4
PbNOF	-0.31	0.62	1.27	indirect	111.5
SiPOF	-0.59	2.04	3.16	indirect	115.9
CNOCl	-0.13	3.64	5.21	indirect	98.4
SiNOCl	-0.99	3.14	4.99	indirect	95.4
GeNOCl	-0.35	2.13	3.59	indirect	96.2
SnNOCl	-0.15	0.62	1.61	direct	94.8
PbNOCl	-0.29	0.16	0.54	direct	106.9
SiPOCl	-0.55	2.42	3.50	indirect	115.2
SiAsOCl	-0.51	2.19	3.13	indirect	118.0
SiSbOCl	-0.39	1.66	2.30	indirect	120.7
SiNSH	-0.66	4.41	5.38	direct	93.4
SiNSeH	-0.54	3.61	4.42	direct	92.2
SiNTeH	-0.34	1.80	2.31	indirect	90.2
SiNSeF	-0.90	1.47	2.18	indirect	94.8
SiNTeF	-1.01	0.64	0.96	indirect	91.0

SiNTeCl	-0.48	0.48	0.87	indirect	92.0

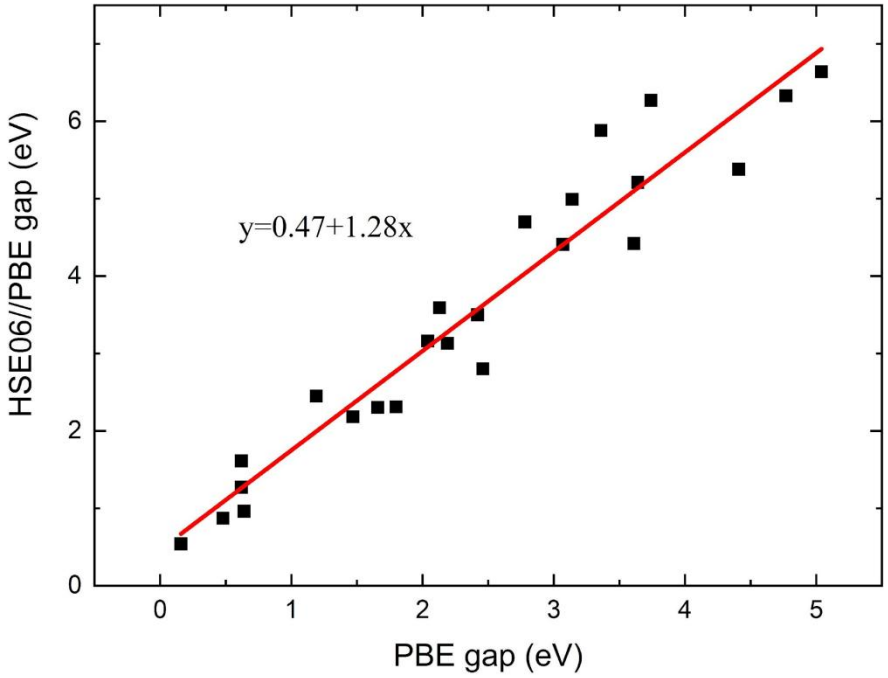

Figure S37 The fitting relationship between the HSE06//PBE gaps and PBE gaps of all 2D *Pca*2$_1$ SiNOX and associated isovalent compounds

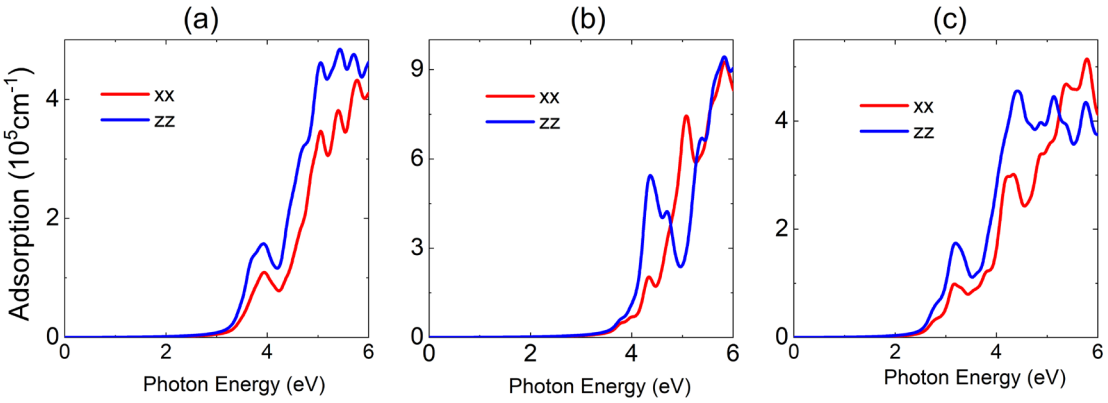

Figure S38 The calculated optical absorptions of 2D (a) *Pca*2$_1$ SiPOH, (b) *Pca*2$_1$ SiAsOCl, and (c) *Pca*2$_1$ SiSbOCl along in-plane spatial directions

S10. References

1. G. Kresse and J. Furthmüller, *Phys. Rev. B*, 1996, **54**, 11169.
2. G. Kresse and J. Furthmüller, *Comput. Mater. Sci*., 1996, **6**, 15-50.
3. P. E. Blöchl, *Phys. Rev. B*, 1994, **50**, 17953.
4. J. P. Perdew, K. Burke and M. Ernzerhof, *Phys. Rev. Lett*., 1998, **80**, 891.
5. S. Grimme, S. Ehrlich and L. Goerigk, *J. Comput. Chem*., 2011, **32**, 1456-1465.
6. J. Neugebauer and T. Hickel, WIRES Comput. *Mol. Sci*., 2013, **3**, 438-448.
7. H. Xiao, J. Tahir-Kheli and W. A. III Goddard, *J. Phys. Chem. Lett.*, 2011, **2**, 212-217.
8. J. Heyd, G. E. Scuseria and M. Ernzerhof, *J. Chem. Phys.*, 2003, **118**, 8207-8215.
9. A. Savin, R. Nesper, S. Wengert and T. F. Fässler, *Angew. Chem. Int. Ed.*, 1997, **36**, 1808-1832.
10. T. A. Manz and N. G. Limas, *RSC Adv.*, 2016, **6**, 47771-47801.
11. K. Momma and F. Izumi, *J. Appl. Crystallogr.*, 2011, **44**, 1272-1276.
12. A. Togo, F. Oba, and I. Tanaka, *Phys. Rev. B*, 2008, **78**, 134106.
13. M. Born, K. Huang and M. Lax, *Am. J. Phys.*, 1955, **23**, 474-474.
14. R. Cowley, *Phys. Rev. B*, 1976, **13**, 4877.
15. F. Mouhat and F.-X. Coudert, *Phys. Rev. B*, 2014, **90**, 224104.
16. Y. Le Page andP. Saxe, *Phys. Rev. B*, 2002, **65**, 104104.
17. C. Jasiukiewicz, T. Paszkiewicz and S. Wolski, *Phys Status Solidi B*, 2008, **245**, 557-561.
18. R. C. Andrew, R. E. Mapasha, A. M. Ukpong and N. Chetty, *Phys. Rev. B*, 2012, **85**, 125428.
19. L. Wang, A.Kutana, X. Zou and B. I. Yakobson, *Nanoscale*, 2015, **7**, 9746-9751.
20. T. Hu, J. Zhou and J. Dong, Phys. Chem. Chem. Phys., 2017, **19**, 21722-21728.
21. Q. Wei, G. Yang and X. Peng, *Phys. Rev. Appl.*, 2020, **13**, 034065.
22. H. Zhang, Z. Fu, D. Legut, T. C. Germann and R. Zhang, *RSC Adv.*, 2017, **7**, 55912-55919.
23. H. C. Andersen, *J. Chem. Phys.*, 1980, **72**, 2384-2393.
24. H. L. Zhuang and R. G.Hennig, *Phys. Rev. B Condens. Matter Mater. Phys.*, 2013, **88**, 115314.
25. B. Meng, T. Jing, and W.-Z. Xiao, *Comput. Mater. Sci.*, 2021, **200**, 110775.
26. A. Laturia, M. L. Van de Put, W. G. Vandenberghe, *NPJ 2D Mater. Appl.*, 2018, **2**, 6.

27. X.-H. Zha, K. Luo, Q. Li, Q. Huang, J. He, X. Wen and S. Du, *EPL*, 2015, **111**, 26007.
28. T. Q. Zhao, Y. J. Sun, Z. G. Shuai and D. Wang, *Chem. Mater.*, 2017, **29**, 6261-6268.
29. N. Wang, H. Gong, Z. Sun, C. Shen, B. Li, H. Xiao, X. Zu, D. Tang, Z. Yin and X. Wu, *ACS Appl. Energy Mater.*, 2021, **4**, 12163-12176.
30. M. Mantina, A. C. Chamberlin, R. Valero, C. J. Cramer and D. G. Truhlar, *J. Phys. Chem. A*, 2009, **113**, 5806-5812.
31. W. Li, J. Carrete, N. A. Katcho and N. Mingo, *Comput. Phys. Commun*., 2014, **185**, 1747-1758.
32. M. Born and K. Huang, *Oxford university press*, 1996.
33. S. Nosé, *J. Chem. Phys*., 1984, **81,** 511-519.
34. T. Akiyama, Y. Tsuboi, K. Nakamura and T. Ito, *J. Cryst. Growth*, 2019, **511**, 89-92.
35. K. Wang, W. Zhou, Y. Cheng, M. Zhang, H. Wang and G. Zhang, *Nanoscale,* 2021, **13**, 10882-10890.
36. D. Li, J. Gao, P. Cheng, J. He, Y. Yin, Y. Hu, L. Chen, Y. Cheng and J. Zhao, *Adv. Func. Mater.*, 2020, **30**, 1904349.
37. K. Gaál-Nagy, *Phys. Rev. B Condens. Matter Mater. Phys.*, 2008, **77**, 024309.

S11 VASP POSCARs of 2D *Pca*2$_1$ SiNOX

SiNOH_POSCAR

1.0

5.6180000305	0.0000000000	0.0000000000
0.0000000000	35.4173011780	0.0000000000
0.0000000000	0.0000000000	4.9488000870

Si	N	O	H
4	4	4	4

Direct

0.392660022	0.017090000	0.546540022
0.607339978	0.982909977	0.046540022
0.892660022	0.982909977	0.546540022
0.107339978	0.017090000	0.046540022
0.369260013	0.003360000	0.210979998
0.630739987	0.996640027	0.710979998
0.869260013	0.996640027	0.210979998
0.130739987	0.003360000	0.710979998
0.911780000	0.936200023	0.573959947
0.088220000	0.063800000	0.073959947
0.411780000	0.063800000	0.573959947
0.588220000	0.936200023	0.073959947
0.322480023	0.076480001	0.430239975
0.677519977	0.923519969	0.930239975
0.822480023	0.923519969	0.430239975
0.177519977	0.076480001	0.930239975

SiNOF_POSCAR

1.0

5.5658998489	0.0000000000	0.0000000000
0.0000000000	36.2501983643	0.0000000000
0.0000000000	0.0000000000	4.9390001297

Si	N	O	F
4	4	4	4

Direct

0.404470026 0.017130001 0.524670005
0.595529974 0.982869983 0.024670005
0.904470026 0.982869983 0.524670005
0.095529974 0.017130001 0.024670005
0.370350003 0.008730000 0.180760026
0.629649997 0.991270006 0.680760026
0.870350003 0.991270006 0.180760026
0.129649997 0.008730000 0.680760026
0.023479998 0.941420019 0.596529961
0.976520002 0.058580000 0.096529961
0.523479998 0.058580000 0.596529961
0.476520002 0.941420019 0.096529961
0.373170018 0.086209998 0.459760010
0.626829982 0.913789988 0.959760010
0.873170018 0.913789988 0.459760010
0.126829982 0.086209998 0.959760010

SiNOCl_POSCAR
1.0
5.4809999466 0.0000000000 0.0000000000
0.0000000000 37.0001983643 0.0000000000
0.0000000000 0.0000000000 4.9306001663
Si N O Cl
4 4 4 4
Direct
0.409410000 0.017650001 0.538589954
0.590590000 0.982349992 0.038589954
0.909410000 0.982349992 0.538589954
0.090590000 0.017650001 0.038589954
0.372110009 0.009900000 0.193650007
0.627889991 0.990100026 0.693650007
0.872110009 0.990100026 0.193650007
0.127889991 0.009900000 0.693650007
0.031700015 0.941969991 0.608890057

0.968299985	0.058030002	0.108890057
0.531700015	0.058030002	0.608890057
0.468299985	0.941969991	0.108890057
0.452799976	0.094599999	0.420599997
0.547200024	0.905399978	0.920599997
0.952799976	0.905399978	0.420599997
0.047200024	0.094599999	0.920599997